Theoretical and Applied Fracture Mechanics 103 (2019) 102252

Contents lists available at ScienceDirect

Theoretical and Applied Fracture Mechanics

journal homepage: www.elsevier.com/locate/tafmec

Phase field fracture in elasto-plastic solids: Abaqus implementation and case studies

Jianguang Fang[a,b,*], Chengqing Wu[a,*], Timon Rabczuk[b], Chi Wu[c], Conggan Ma[d], Guangyong Sun[c], Qing Li[c]

[a] School of Civil and Environmental Engineering, University of Technology Sydney, Sydney, NSW 2007, Australia
[b] Institute of Structural Mechanics, Bauhaus-University Weimar, 99423 Weimar, Germany
[c] School of Aerospace, Mechanical and Mechatronic Engineering, The University of Sydney, Sydney, NSW 2006, Australia
[d] School of Automotive Engineering, Harbin Institute of Technology, Weihai, China

ARTICLE INFO

Keywords:
Phase field fracture
Plasticity
UEL
UMAT
Staggered solution
Crack propagation

ABSTRACT

Phase field modelling for fracture has been extended from elastic solids to elasto-plastic solids. In this study, we present the implementation procedures of a staggered scheme for phase field fracture of elasto-plastic solids in commercial finite element software Abaqus using subroutines UEL and UMAT. The UMAT is written for the constitutive behaviour of elasto-plastic solids, while the UEL is written for the phase field fracture. The phase field and displacement field are solved separately using the Newton-Raphson iteration method. In each iteration, one field is computed by freezing the other field at the last loading increment. A number of benchmark examples are tested from one single element up to 3D problems. The correctness of the staggered scheme is verified analytically in terms of the stress-strain curve and the evolution of the phase field in the one single element example. In the 2D and 3D problems, the fracture behaviour of elasto-plastic solids can be reproduced in terms of reaction force curve and crack propagation, which exhibit good agreement with the experimental observations and numerical results in literature. Not only can the proposed implementation help attract more academic researchers, but also engineering practitioners to take the advantages of phase field modelling for fracture in elasto-plastic solids. The Abaqus subroutine codes can be downloaded online from Mendeley data repository linked to this work (The link is provided in Supplementary material).

1. Introduction

Fracture is one of the most common failure modes in engineering practice. Numerical analysis of fracture-induced failure is crucial for the design of materials and structures, to maintain their load-carrying capacity. Numerical techniques for modelling fracture may be categorised into two groups depending upon how they handle the discontinuity: namely discrete and diffuse/smear methods.

Discrete methods describe complex crack geometry in a discrete manner, such as node splitting [1], cohesive surfaces [2], hybrid discrete and finite element (FE) methods [3]. Often, the crack can only propagate between elements using these methods; and thus the results are highly mesh-dependent. To address this issue, remeshing strategies at the location where the material is broken were proposed to capture the discontinuous crack geometry [4–6]. An alternative is to resort to the extended finite element method (XFEM) [7,8], in which a local enrichment in the shape functions is used to model the jumps in the displacement field, thereby avoiding remeshing the cracked domain. Nevertheless, algorithmic tracking of the evolution of complex fracture surfaces is a tedious task in the numerical implementation. The cracking particles method (CPM) [9–11] is also a discrete crack method but it does not require any explicit representation of the crack surface and any crack tracking algorithms.

Diffuse methods for fracture modelling are based upon the assumption that the discontinuity in the cracked material is not sharp but can be interpreted as smeared damage. A recently emerged approach, the phase field method, has been attracting much attention because of its simplicity for numerical implementation. In the phase field model, a smooth boundary of the phase field is employed to approximate the internal discontinuity boundary of a crack. The use of the phase field model for fracture can circumvent the complexity of tracking crack propagation that is typically required in discrete models.

Phase field modelling for brittle fracture have been developed by numerous researchers in the last two decades. It originated from the

* Corresponding authors at: School of Civil and Environmental Engineering, University of Technology Sydney, Sydney, NSW 2007, Australia (J. Fang).
E-mail addresses: Jianguang.Fang@uts.edu.au (J. Fang), Chengqing.Wu@uts.edu.au (C. Wu).

https://doi.org/10.1016/j.tafmec.2019.102252
Received 10 December 2018; Received in revised form 13 May 2019; Accepted 15 May 2019
Available online 17 May 2019
0167-8442/

variational formulation of brittle fracture by Francfort and Marigo [12] and the regularised formulation by Bourdin et al. [13] that is more suitable for numerical implementation. Since then, the phase field modelling has demonstrated its ability to predict various brittle fracture problems such as quasi-static [14] and dynamic [15,16] brittle fracture. It has proven a powerful and robust tool to reproduce complex crack patterns, including crack initiation, crack branching and determination of unknown crack paths [17–24]. Recently, phase field modelling has also been used in topology optimization to maximise fracture resistance of brittle materials [25,26].

Attributable to the smooth feature, the phase field modelling for brittle fracture can be implemented flexibly in any finite element codes or commercial programs. The implementation in commercially available software enables not only research academics but also engineering practitioners to take the advantages of phase field modelling for fracture. In this regard, Msekh et al. [27] presented an Abaqus implementation of phase field fracture via a user-defined element (UEL) subroutine, where the coupled nonlinear system consisting of the linear momentum equation and the phase field evolution equation is solved iteratively in a monolithic manner using the Newton Raphson method. Molnár and Gravouil [28] implemented a new staggered (decoupled) phase field model for brittle fracture in Abaqus, where two element layers were used with each contributing to different degrees of freedom. In their method, the displacement field and phase field were solved iteratively based upon the value of the other field taken from the last time increment. Liu et al. [29] provided an Abaqus implementation of monolithic and staggered phase field models to solve quasi-static and dynamic fracture problems. The monolithic and staggered algorithms were implemented via UEL and user-defined material (UMAT/VUMAT), respectively. Zhou et al. [30] presented a novel implementation of phase field modelling for brittle fracture in COMSOL that has advantages in supporting the programming of multi-field problems, because phase field modelling for brittle fracture is characterised with multiple fields in nature even for a purely mechanical problem. Most recently, Seleš et al. [31] proposed a creative staggered algorithm with residual control in Abaqus implementation. The algorithm exhibited considerable advantages in computational efficiency and accuracy, and the results were not dependent on the selection of loading increment.

The above implementations of phase field modelling in commercial software Abaqus and COMSOL are limited to brittle fracture in elastic solids. However, it is crucial to take into account plasticity in constitutive modelling. One of the reasons is that even for brittle materials such as plain concrete, certain permanent deformation can be observed after unloading. It can be modelled with the classical plasticity theory in a phenomenological fashion [32,33]. Consequently, the phase field modelling for fracture has been coupled with plasticity to capture the mechanical response of elasto-plastic solids. For example, Miehe and co-workers [34–36] proposed a phase-field model to reproduce the experimental observation of the failure mode transition from ductile fracture to brittle fracture. Duda et al. [37] presented a phase field formulation for fracture of elasto-plastic solids subject to small strains. The elastic and fracture energies took the classical forms used in the brittle fracture formulations, while the plastic energy was expressed in terms of the accumulated plastic strain. Ambati et al. [38] coupled the evolution of the phase field with the accumulation of plastic strains by introducing a variable that reflected the accumulation of plastic strains into the elastic degradation function. Borden et al. [39] developed a phase field model for fracture in ductile materials under large strains, where a threshold of plastic work was introduced to control the contribution of plastic deformation to crack growth. Alessi et al. [40] studied the coupling technique of the phase field damage and plasticity for one-dimensional examples, in which four different macroscopic responses were identified by tuning the key constitutive parameters. Alessi et al. [41] conducted a critical review of phase-field models for fracture coupled with plasticity; and all the models were compared after being cast in the same variational framework. Rodriguez et al. [42] proposed a rigorous variational approach to the phase field modelling of brittle and ductile fracture, where several dissipative mechanisms were introduced. Fang et al. [43] proposed a variational formulation for phase field modelling of fracture coupled with multi-surface plasticity; and the effects of plasticity yield functions and hardening on material behaviour were analysed.

It is noted that most of these above-mentioned studies were based upon in-house finite element codes, which may limit practical applications of phase field modelling for fracture in engineering practice. This article aims to report the implementation of phase field modelling for elasto-plastic solids in commercial software Abaqus. The phase field fracture problem in elasto-plastic solids is solved using a staggered algorithm which decouples the phase field and the displacement field; and the staggered algorithm is implemented via Abaqus UEL and UMAT subroutines. The remainder of this study is structured as follows: Section 2 presents the phase field model of fracture for elasto-plastic solids, followed by numerical implementation in Abaqus in Section 3. Then, Section 4 provides some numerical examples from one single element, to 2D and 3D cases. Last, conclusions are drawn in Section 5.

2. Phase field model of fracture for elasto-plastic solids

Consider an arbitrary body Ω with external boundary $\partial\Omega$ and internal discontinuity boundary Γ as in Fig. 1a. The whole external boundary is decomposed into $\partial\Omega = \partial\Omega^s + \partial\Omega^h$ and $\partial\Omega^s \cap \partial\Omega^h = \varnothing$. The body is fixed on the essential boundary $\partial\Omega^h$ and applied a surface-traction on the boundary $\partial\Omega^s$. The internal discontinuity boundary Γ represents a set of discrete cracks. In accordance with Griffith's theory of brittle fracture, the energy required to create a unit area of facture surface is equal to the critical fracture energy density g_f. To circumvent the problems of tracking the propagating discontinuity, the fracture surface is approximated by a phase field variable $d\,(0 \le d \le 1)$ in the phase field fracture context (see Fig. 1b). The value of this phase field d is equal to 0 for a completely intact state of the material and is equal to

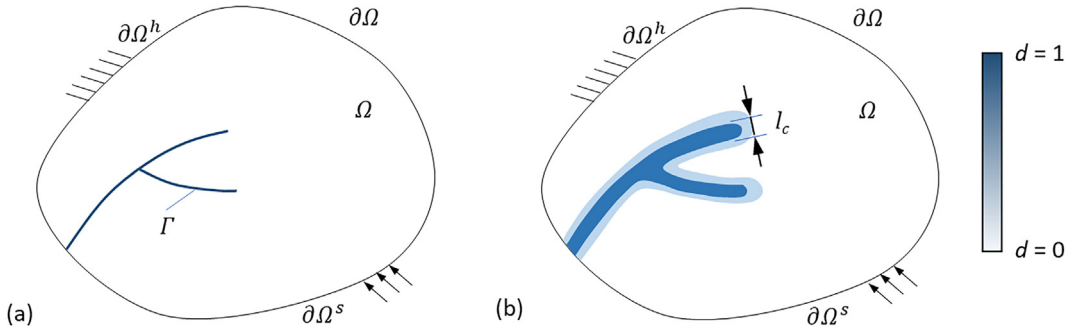

Fig. 1. (a) Schematic representation of a solid body with internal discontinuity boundary Γ; (b) Approximation of the internal discontinuity boundary by the phase-field d. The length scale parameter l_c controls the width of the failure zone.

1 for a fully broken state.

The fracture energy can be approximated by [13]:

$$\int_\Gamma g_f \mathrm{d}\Gamma = \int_\Omega \frac{g_f}{2l_c}[l_c^2 \nabla d \cdot \nabla d + d^2]\mathrm{d}\Omega \tag{1}$$

The total energy functional of the elasto-plastic solids may be then defined as [43],

$$\Pi = \int_\Omega (1-d)^2\left(\frac{1}{2}\boldsymbol{\varepsilon}^{\mathrm{e}}\colon \bar{\boldsymbol{\sigma}} + \frac{1}{2}\bar{H}\gamma^2 + \bar{\sigma}_y\gamma\right)\mathrm{d}\Omega + \int_\Omega \frac{g_f}{2l_c}(l_c^2\nabla d\cdot\nabla d + d^2)\mathrm{d}\Omega - \int_\Omega \mathbf{b}\cdot\mathbf{u}\mathrm{d}\Omega - \int_{\partial\Omega^{\mathrm{s}}} \mathbf{t}\cdot\mathbf{u}\mathrm{d}\partial\Omega \tag{2}$$

where $\mathbf{t}$ is the external traction applied on $\partial\Omega^{\mathrm{s}}$, and $\mathbf{b}$ is the external body force. The last two terms on the right-hand side of Eq. (2) are the work done by the external forces. The first term is the strain energy due to elastic and plastic deformations of the damaged materials, where "-" represents the effective (undamaged) quantities in continuum damage mechanics. $\bar{\boldsymbol{\sigma}}$, $\bar{H}$ and $\bar{\sigma}_y$ are named as the effective (undamaged) stress tensor, effective hardening modulus and effective yield stress, respectively. γ is the accumulated plastic strain. The relationship between effective stress and nominal stress may be expressed as: $\boldsymbol{\sigma}(d) = (1-d)^2\bar{\boldsymbol{\sigma}}$.

The aim of formulating the energy functional is to find the state variables $(\mathbf{u}, \gamma, d)$ by using the energetic principles. The governing equations and evolution laws for the elasto-plastic-damage problem can be derived as in Table 1 [43].

To simplify the treatment of the phase field equations, a history field function is defined as follows [39]:

$$\mathcal{H} := \max_{\tau\in[0,t]}\left(\frac{1}{2}\boldsymbol{\varepsilon}^{\mathrm{e}}\colon \bar{\boldsymbol{\sigma}}\right) + \frac{1}{2}\bar{H}\gamma^2 + \bar{\sigma}_y\gamma \tag{3}$$

Then, the phase field problem may be solved by using Eq. (4) instead of the damage Karush–Kuhn–Tucker (KKT) conditions.

$$2(1-d)\mathcal{H} + \frac{g_f}{l_c}(l_c^2\Delta d - d) = 0 \tag{4}$$

3. Numerical implementation in Abaqus

In this section, finite element discretisation is given for phase field fracture of elasto-plastic solids. For convenience, a matrix notation is used in this section. A mixed finite element for displacement field $\mathbf{u}$ and phase field d is proposed here. The spatial discretisation is considered as follows:

Table 1
Governing equations and evolution laws.

Equilibrium	
Equilibrium equation	$\mathrm{div}\ \boldsymbol{\sigma} = \boldsymbol{b}\ \ \mathrm{in}\ \ \Omega$
Boundary conditions	$\begin{cases} \boldsymbol{n}\cdot\boldsymbol{\sigma} = \boldsymbol{t} & \mathrm{on}\ \ \partial\Omega^{\mathrm{s}} \\ \mathbf{u} = \mathbf{u} & \mathrm{on}\ \ \partial\Omega^{\mathrm{h}} \end{cases}$
Plasticity conditions	
KKT conditions	$\begin{cases} \dot{\gamma} \geq 0 \\ \bar{f}^p(\mathbf{u},\gamma) \leq 0 \quad \mathrm{in}\Omega \\ \bar{f}^p(\mathbf{u},\gamma)\dot{\gamma} = 0 \end{cases}$
Flow rule	$\dot{\boldsymbol{\varepsilon}}^{\mathrm{p}} = \dot{\gamma}\mathbf{a}\ \ \mathrm{in}\ \ \Omega$
Yield surface	$\bar{f}^p(\mathbf{u},\gamma,d) := \bar{\sigma}^{\mathrm{eq}}(\mathbf{u},\gamma) - \bar{H}\gamma - \bar{\sigma}_y$
Damage conditions	
KKT conditions	$\begin{cases} \dot{d} \geq 0 \\ f^d(\mathbf{u},\gamma,d) \leq 0 \quad \mathrm{in}\Omega \\ f^d(\mathbf{u},\gamma,d)\dot{d} = 0 \end{cases}$
Yield surface	$f^d(\mathbf{u},\gamma,d) := (1-d)(\varepsilon^e\colon \bar{\sigma} + \bar{H}\gamma^2 + 2\bar{\sigma}_y\gamma) + \frac{g_f}{l_c}(l_c^2\Delta d - d)$
Boundary condition	$\mathbf{n}\cdot\nabla\ \mathrm{d} \geqslant 0\ \mathrm{on}\ \partial\Omega$

$$\mathbf{u} = \sum_{i=1}^{N_{node}} \mathbf{N}_i^{\mathbf{u}}\mathbf{u}_i, \qquad d = \sum_{i=1}^{N_{node}} N_i d_i \tag{5}$$

where $\mathbf{N}_i^{\mathbf{u}}$ and $N_i(\mathbf{x})$ stand for the shape functions associated with node i; and $\mathbf{u}_i$ and d_i are the displacement field and phase field values at node i, respectively. N_{node} is the number of nodes in the finite elements. The corresponding derivatives can be given by:

$$\boldsymbol{\varepsilon} = \sum_{i=1}^{N_{node}} \mathbf{B}_i^{\mathbf{u}}\mathbf{u}_i, \qquad \nabla d = \sum_{i=1}^{N_{node}} \mathbf{B}_i^d d_i \tag{6}$$

where $\mathbf{B}_i^{\mathbf{u}}(\mathbf{x})$ and $\mathbf{B}_i^d(\mathbf{x})$ are the matrices with spatial derivatives of the corresponding shape functions.

The test functions and their derivatives can be discretised as:

$$\delta\mathbf{u} = \sum_{i=1}^{N_{node}} \mathbf{N}_i^{\mathbf{u}}\delta\mathbf{u}_i, \qquad \delta d = \sum_{i=1}^{N_{node}} N_i\delta d_i$$

$$\delta\boldsymbol{\varepsilon} = \sum_{i=1}^{N_{node}} \mathbf{B}_i^{\mathbf{u}}\delta\mathbf{u}_i, \qquad \nabla\delta d = \sum_{i=1}^{N_{node}} \mathbf{B}_i^d\delta d_i \tag{7}$$

The residual vectors for the displacement and phase fields read as:

$$\mathbf{r}_i^{\mathbf{u}} = \int_\Omega (1-d)^2(\mathbf{B}_i^{\mathbf{u}})^{\mathrm{T}}\boldsymbol{\sigma}\mathrm{d}\Omega - \int_\Omega (\mathbf{N}_i^{\mathbf{u}})^{\mathrm{T}}\mathbf{b}\mathrm{d}\Omega - \int_{\partial\Omega} (\mathbf{N}_i^{\mathbf{u}})^{\mathrm{T}}\mathbf{h}\mathrm{d}\partial\Omega$$

$$r_i^d = \int_\Omega \left\{\left[\frac{g_f}{l_c}d - 2(1-d)\mathcal{H}\right]N_i + g_f l_c(\mathbf{B}_i^d)^{\mathrm{T}}\nabla d\right\}\mathrm{d}\Omega \tag{8}$$

The system of equations is nonlinear due to the phase field crack and plasticity so that one must resort to incremental-iterative schemes. The Abaqus implementation is able to take advantage of its built-in nonlinear solver and its automatic time-stepping schemes. To decouple the phase field and displacement field, we adopt a staggered algorithm to solve the problem. The displacement field can be solved by freezing the phase field at the last loading increment. Meanwhile, the phase field can be solved by freezing the displacement field and internal plastic parameters at the last loading increment. The corresponding Newton-Raphson iteration may be written as,

$$\begin{Bmatrix}\mathbf{u}\\ d\end{Bmatrix}_{n+1} = \begin{Bmatrix}\mathbf{u}\\ d\end{Bmatrix}_n - \begin{bmatrix}\mathbf{K}^{\mathbf{uu}} & 0\\ 0 & \mathbf{K}^{dd}\end{bmatrix}^{-1}\begin{Bmatrix}\mathbf{r}^{\mathbf{u}}\\ r^d\end{Bmatrix}_n \tag{9}$$

in which

$$\mathbf{K}_{ij}^{\mathbf{uu}} = \frac{\partial\mathbf{r}_i^{\mathbf{u}}}{\partial\mathbf{u}_j} = \int_\Omega [(1-d)^2 + k](\mathbf{B}_i^{\mathbf{u}})^{\mathrm{T}}\mathbf{E}^{\mathrm{epc}}\mathbf{B}_j^{\mathbf{u}}\mathrm{d}\Omega \tag{10a}$$

$$\mathbf{K}_{ij}^{dd} = \frac{\partial r_i^d}{\partial d_j} = \int_\Omega \left\{g_f l_c(\mathbf{B}_i^d)^{\mathrm{T}}\mathbf{B}_j^d + \left[\frac{g_f}{l_c} + 2\mathcal{H}\right]N_i N_j\right\}\mathrm{d}\Omega \tag{10b}$$

where $\mathbf{E}^{\mathrm{epc}}$ is the consistent Jacobian matrix.

To implement the solution in Abaqus/Standard, a two-layer structure is employed as shown in Fig. 2. Each layer shares the same nodes but contributes to the stiffness of different degrees of freedom (DOF). The elements in the first layer have two displacement DOFs for 2D or three DOFs for 3D problems; while the elements in the second layer have only one phase field DOF. The user-defined subroutine UMAT is called at each Gauss point in the first layer and UEL is called at each element in the second layer. The constitutive behaviour at the elemental Gauss points is evaluated in UMAT for the displacement field. Specifically, the stress and consistent Jacobian at Gauss points are evaluated for the plasticity model. Note that the use of identical elastic and plastic degradation functions $(1-d)^2$ in Eq. (2) allows a straightforward use of standard elasto-plastic algorithms [43]. Any plasticity models can be implemented via a UMAT subroutine; and the widely used J_2 plasticity is considered in this study. The corresponding two elements in the two layers share information via a common block. Table 2 lists six variables stored in the common block. A number of quantities as shown in Table 3 are stored as solution-dependent state variables STATEV in UMAT, which can be post-processed in Abaqus/CAE.

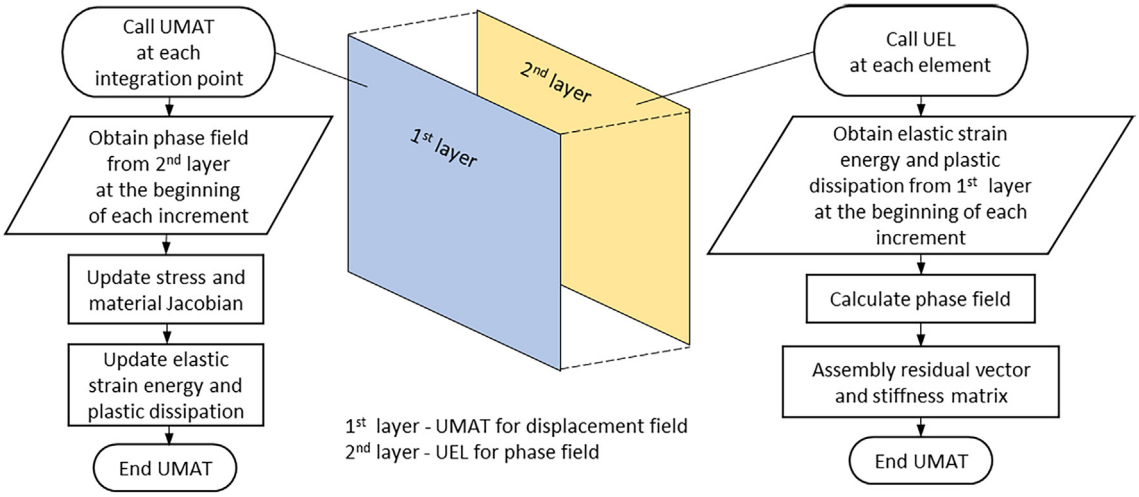

Fig. 2. Two-layer structure of Abaqus subroutines.

Table 2
Information in the common block.

Number	Variables
	UMAT
1	Phase field
2	Elastic strain energy
3	Plastic dissipation
	UEL
4	Phase field
5	Elastic strain energy
6	Plastic dissipation

Table 3
Solution-dependent state variables in UMAT.

Variable	STATEV numbering in UMAT	
	2D	3D
Elastic strains	STATEV1-STATEV4	STATEV1-STATEV6
Plastic strains	STATEV5-STATEV8	STATEV7-STATEV12
Undegraded stresses	STATEV9-STATEV12	STATEV13-STATEV18
Equivalent plastic strain	STATEV13	STATEV19
Elastic strain energy	STATEV14	STATEV20
Plastic dissipation	STATEV15	STATEV21
Phase field	STATEV16	STATEV22

4. Numerical examples

In all the modelling cases below, the isoparametric elements are used for discretisation with four nodes for 2D problems or eight nodes for 3D problems. The following material parameters are adopted unless otherwise stated [38]: Young's modulus $E = 71.48$ GPa, Poisson ratio $\nu = 0.3$, initial yield stress $\sigma_{y0} = 345$ MPa, critical fracture energy density $g_f = 9.31$ MPa mm, hardening modulus $H = 714.8$ MPa. The single element is first used to verify the proposed staggered algorithm against the analytic solution. Then, three 2D examples under plane strain condition are presented to demonstrate the capacity of the proposed algorithm. Finally, two 3D problems are employed to model 3D crack propagation in elasto-plastic solids.

The corresponding subroutine FORTRAN codes and Abaqus input files can be downloaded from the link provided in Supplementary data. A tutorial is also provided in Appendix A for further explaining how to use the codes for solving the numerical problems.

4.1. One element

One 3D brick element subject to uniaxial tension is used to understand the phase field model for fracture analysis in elasto-plastic solids. The length scale parameter l_c is set to be 1.0 mm. The dimensions of the cube element are $1 \times 1 \times 1$ mm. Fig. 3a shows the applied loading and the geometry. The applied displacements at the top and bottom surfaces are $u = 0.075$ mm.

The gradient in the phase field vanishes because it is uniform in the element. Neglecting the irreversibility of crack growth, the history strain energy $H = \int_0^{\bar{\varepsilon}} \bar{\sigma} d\bar{\varepsilon}$ is the area under the axial stress-strain curve, which can be formulated as:

$$\mathcal{H} = \begin{cases} \bar{E}\bar{\varepsilon}^2/2, & \bar{\varepsilon} \le \varepsilon_y \\ \bar{E}\varepsilon_y^2/2 + \bar{\sigma}_y(\bar{\varepsilon} - \varepsilon_y) + \bar{K}(\bar{\varepsilon} - \varepsilon_y)^2/2, & \bar{\varepsilon} > \varepsilon_y \end{cases} \tag{11}$$

where $\bar{E}$ is the effective Young's modulus, $\varepsilon_y = \bar{\sigma}_y/\bar{E}$ is the strain at the onset of yielding, and $\bar{K} = \bar{E}\bar{H}/(\bar{E} + \bar{H})$ is the effective tangential modulus. The phase field can be then calculated from Eq. (4)

$$d = \frac{2\mathcal{H}}{g_f/l_c + 2\mathcal{H}} \tag{12}$$

The stress may be expressed as:

$$\sigma = (1-d)^2\bar{\sigma} = \begin{cases} (1-d)^2\bar{E}\varepsilon, & \varepsilon < \varepsilon_y \\ (1-d)^2(\bar{\sigma}_y + \bar{K}(\varepsilon - \varepsilon_y)), & \varepsilon \ge \varepsilon_y \end{cases} \tag{13}$$

Fig. 3 compares the analytic and numerical solutions. It can be seen that the numerical solution agrees well with the analytic solution in terms of the calculated stress and phase field of damage. Furthermore, the evolution of the phase field obtained from the staggered algorithm as shown in Fig. 3b satisfies the irreversibility criterion without any penalty parameter as used in the monolithic scheme [27]. In addition to stiffness degradation, permanent (plastic) deformation can be observed after unloading (as shown in Fig. 3a), which is attributable to the coupling effect with plasticity. The necessity of coupling damage mechanics with plasticity has proven even for brittle materials such as concrete [44–47]. Fig. 3c presents the relative errors of the numerically calculated stresses. If the displacement is loaded in $\Delta u = 7.5 \times 10^{-5}$ mm $\times$ 1000 steps, the error is less than 4%, which is consistent with the results reported in [28]. The error will even decrease if the displacement is loaded in $\Delta u = 3.75 \times 10^{-5}$ mm$\times$ 2000 steps.

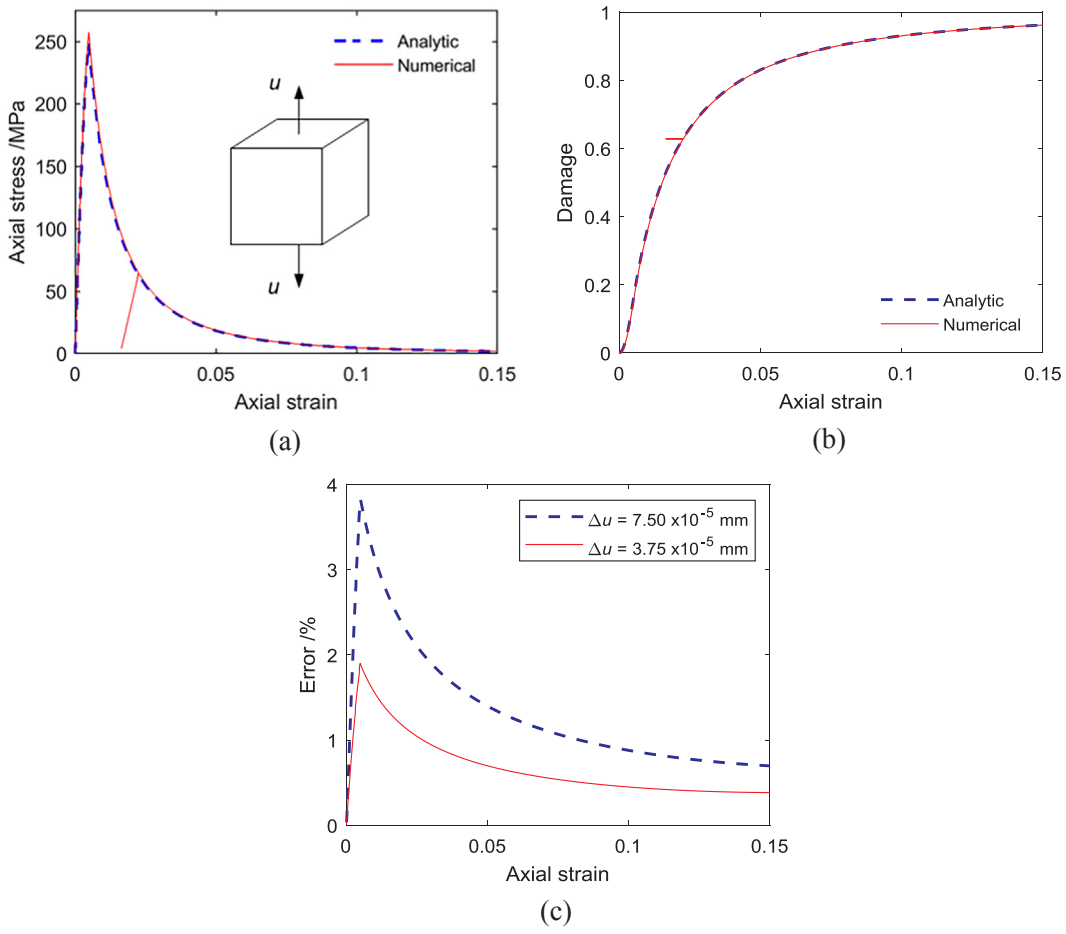

Fig. 3. Comparison of numerical and analytic solutions: (a) Axial stress, (b) Phase-field damage and (c) Errors of numerical solutions.

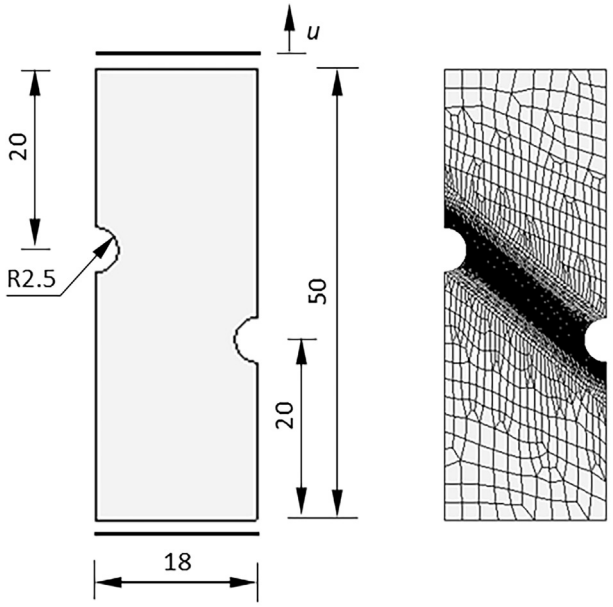

Fig. 4. Geometry and finite element model of the axisymmetrically notched.

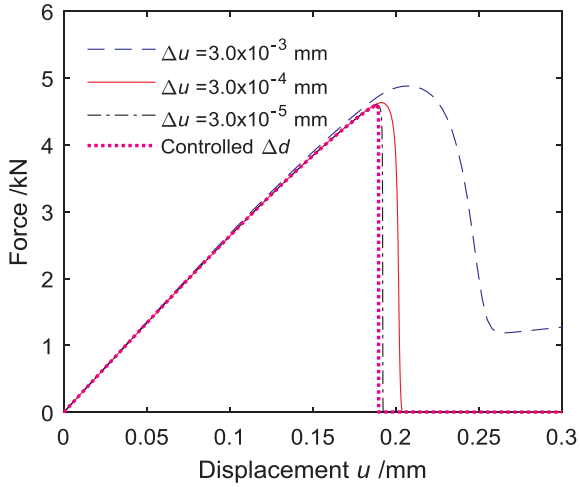

Fig. 5. Force versus displacement curves of using different loading increments for the axisymmetrically notched specimen.

4.2. Axisymmetrically notched specimen

We examine the axisymmetrically notched specimen in this example. Fig. 4 illustrates the geometry and finite element model of the specimen. The length scale parameter l_c is set to be 0.2 mm and the

Table 4
Computational costs of using different loading increments for the axisymmetrically notched specimen.

Automatic stepping with $\Delta d \leq 0.001$	Uniform increment size Δu		
	3.0×10^{-3} mm	3.0×10^{-4} mm	3.0×10^{-5} mm
1677 s	214 s	2092 s	18,708 s

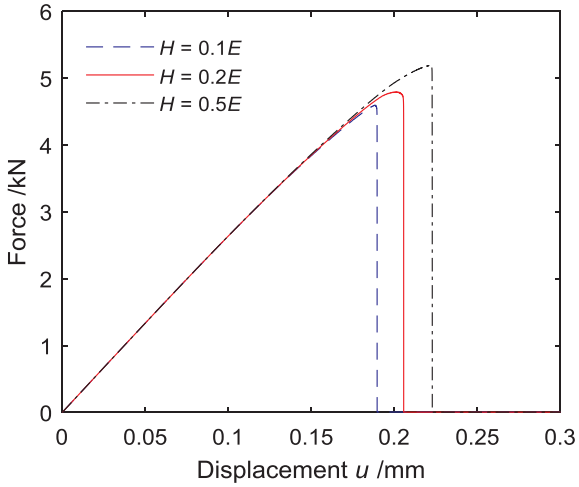

Fig. 6. Force versus displacement curves of different hardening specimens for the axisymmetrically notched specimen.

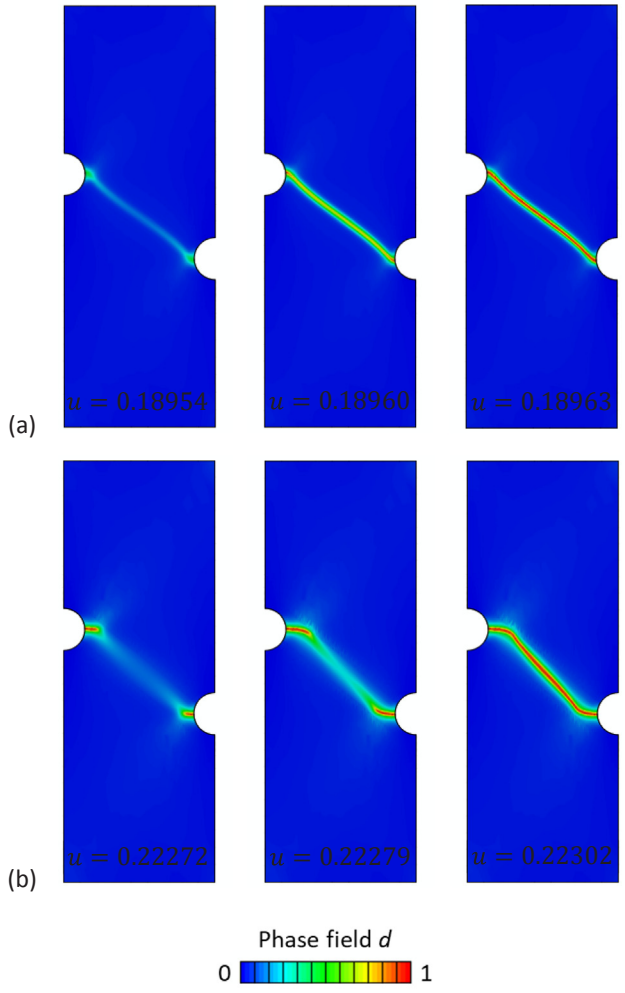

Fig. 7. Crack propagation of the flat grooved specimen for different hardenings: (a) $H = 0.1E$, and (b) $H = 0.5E$.

thickness of the specimen is 1.0 mm. The mesh is refined in the area where the crack is expected to develop. The top edge is restrained horizontally and displaced vertically while the bottom edge is fully fixed.

The reaction force at the bottom edge of the specimen is provided in

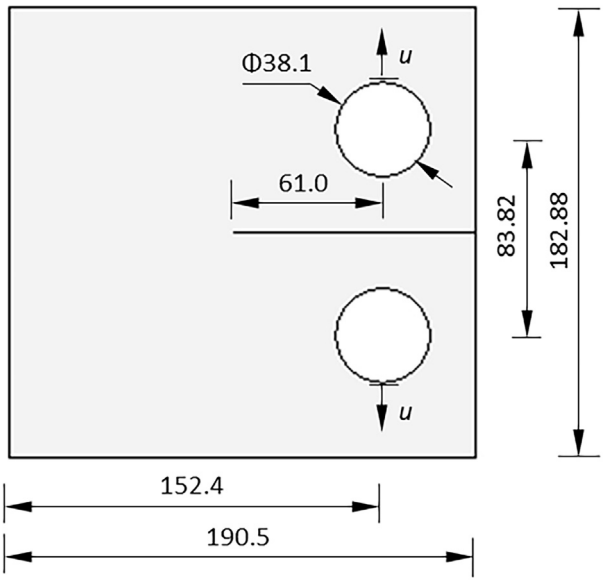

Fig. 8. Geometry of the compact tension specimen.

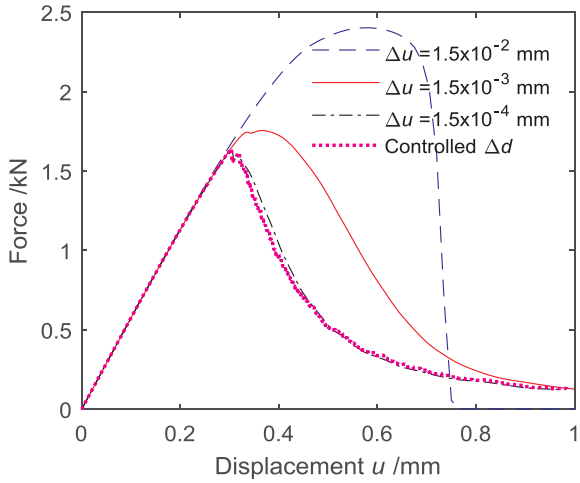

Fig. 9. Force versus displacement curves of using different loading increments for the compact tension specimen.

Table 5
Computational costs of using different loading increments for the compact tension specimen.

Automatic stepping with $\Delta d \leq 0.01$	Uniform loading increment size Δu		
	1.5×10^{-2} mm	1.5×10^{-3} mm	1.5×10^{-4} mm
17,503 s	403 s	4319 s	37,067 s

Fig. 5. The increment size of loading displacement Δu would have a significant effect on the force response. With the decrease in the incremental size, the reduction of the maximum force can be observed, and the force starts to decrease more sharply in the post-peak region. When the increment of loading displacement is small enough ($\Delta u < 3.0 \times 10^{-5}$ mm), the convergence of the result is observed. This is consistent with the results in the literature [28], in which although the staggered algorithm is robust for the phase field fracture problems, it does need a relatively small increment to obtain a converged result. While it may be possible to develop a residual controlled staggered algorithm for Abaqus implementation [31], a practical strategy adopted here is to control the maximum change in the phase field value at

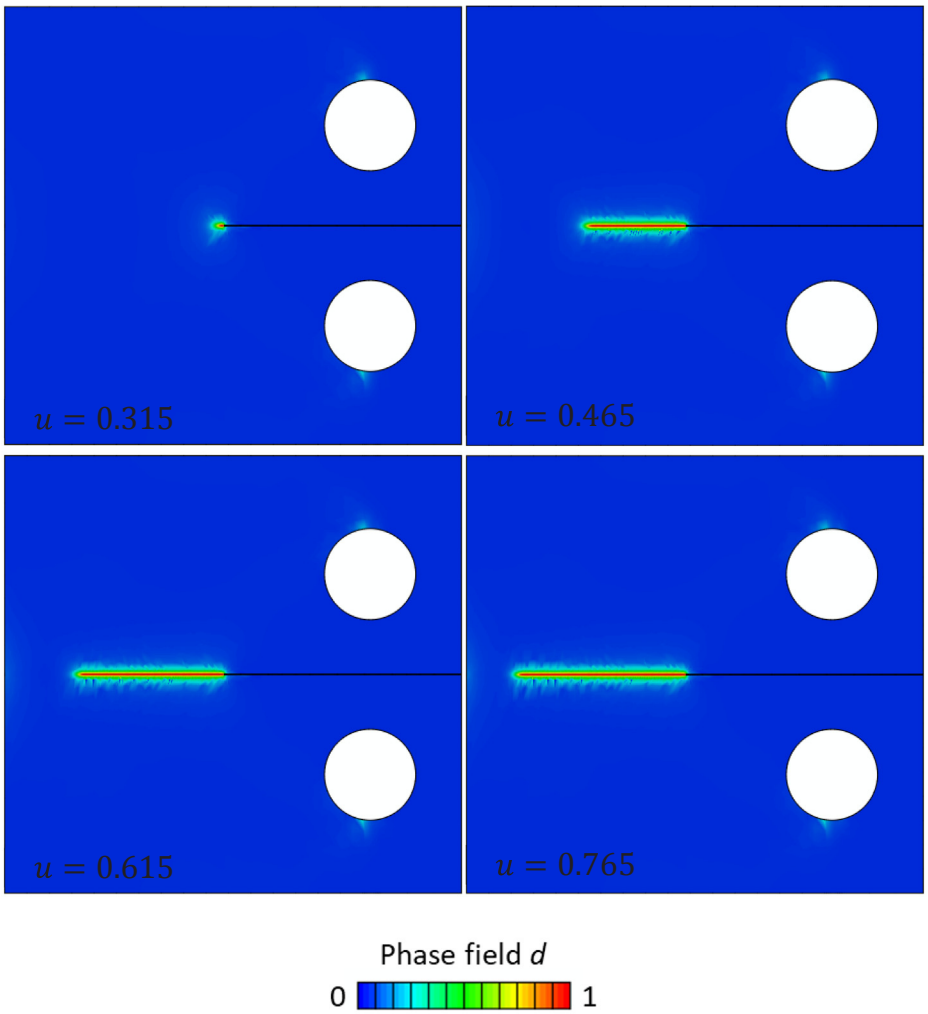

Fig. 10. Crack propagation of the compact tension specimen.

integration points. Specifically, when the change in the phase field value is too large, the size of the next loading increment is reduced to slow down the cracking process. Table 4 shows the computational cost using different loading increments. The simulations are performed on an Intel® Core™ i5-6300U CPU @ 2.40 GHz with 8 GB RAM memory. Together with Fig. 5, it can be found that limiting the change in the phase-field value may help to obtain a converged result and save computational cost.

Fig. 6 exhibits that a greater hardening modulus would lead to a larger maximum force, and thus the specimen experiences a larger ultimate deformation. Interestingly, the hardening modulus (H) may also influence the crack trajectory (Fig. 7). For the specimen with $H = 0.1E$, the cracks initiate at both the notches, and develop diagonally across the specimen. For the specimen with $H = 0.5E$, the crack propagates horizontally first before developing diagonally until being fully damaged.

4.3. Compact tension specimen

A case of compact tension is studied in this example. As shown in Fig. 8, a prescribed open crack is placed horizontally in the plate. The length scale parameter l_c is set to 0.15 mm and the thickness of the specimen is 1.0 mm. The tensile forces exerted by the two loading pins on the specimen holes are modelled by prescribing the displacements (u) at the top and bottom nodes of the holes.

Fig. 9 and Table 5 compare the force-displacement curves and computational costs of using different loading increments, respectively. Again, the control of the change in the phase field value is helpful to obtain a converged result and save CPU time. Fig. 10 illustrates the evolution of the phase field damage. The crack initiates at the notch tip and propagates in a straight line horizontally.

4.4. Flat grooved specimen

The tensile test on a flat grooved specimen is investigated in this example; and Fig. 11 shows the geometry, boundary condition and finite element model of the specimen. The top end of the specimen is vertically loaded in displacement whilst the bottom end is fully fixed. The length scale parameter l_c is set to be 0.1 mm and the thickness of the specimen is 1.0 mm.

Fig. 12a compares the responses under different hardening moduli. With the increase in hardening modulus, the specimen produces a larger maximum force and undergoes larger plastic deformation. Fig. 12b exhibits that the length scale parameter could also considerably influence the response.

Fig. 13 graphs the cracking processes, where the crack initiates at the specimen centre, then propagates in the direction about 45° to the loading direction. The numerical results are consistent with the experimental observation that the specimen at the end of the test shows a slant cracked surface [48].

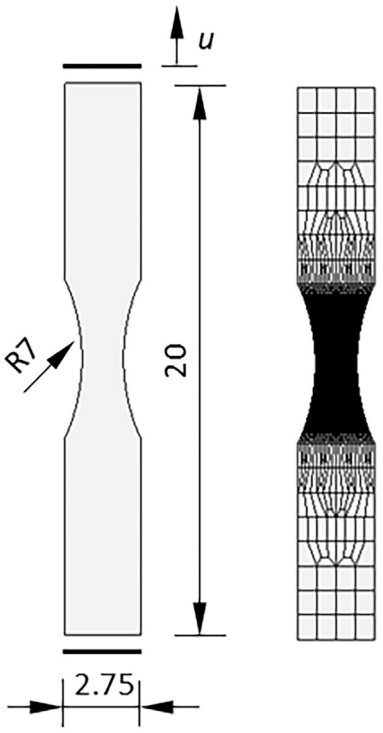

Fig. 11. Geometry and finite element model of the flat grooved specimen.

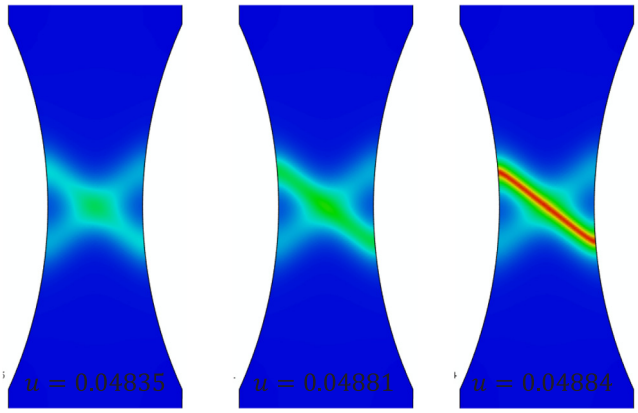

Fig. 13. Crack propagation of the flat grooved specimen.

4.5. Four-point bending of a 3D notched beam

To demonstrate the ability of the proposed algorithm to predict the crack propagation in three-dimensional (3D) scenarios, the four-point bending of a notched beam is modelled as shown in Fig. 14. The beam is supported by two rollers on the bottom surface and is loaded in two prescribed displacements on the top surface. The length scale parameter l_c is set to be 0.1 mm. The mesh is refined in the area where the crack is expected to develop. The loading increment is set to $\Delta u = 8.0 \times 10^{-4}$ mm.

To show the crack, the isosurface of the phase-field damage is depicted with a value greater than 0.95 in Fig. 15. The crack initiates at the notch tip and then propagates upwards. Fig. 16 shows the reaction force at the supports versus the mid-span deflection under cyclic loading. Stiffness degradation can be observed from the unloading stage as result of the phase field damage occurring in the beam. Moreover, residual deformation can be seen when the force unloads to zero

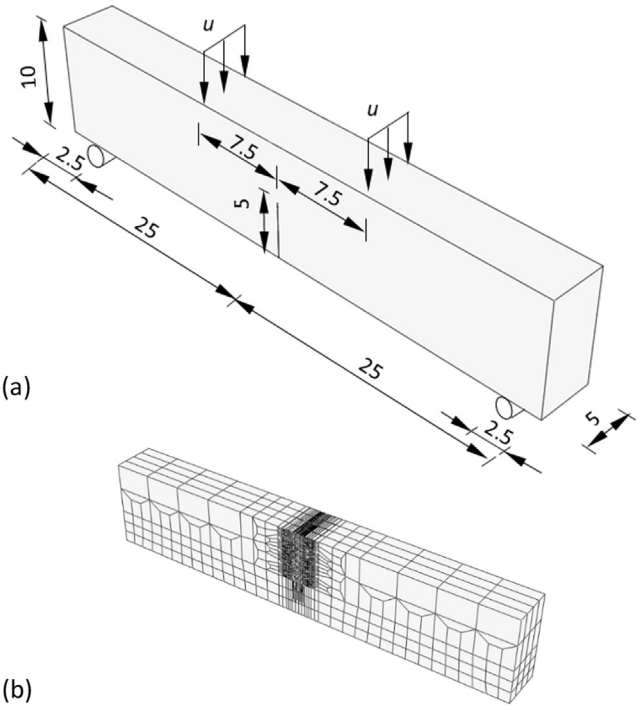

Fig. 14. 3D notched beam under four-point bending: (a) geometry and (b) finite element model.

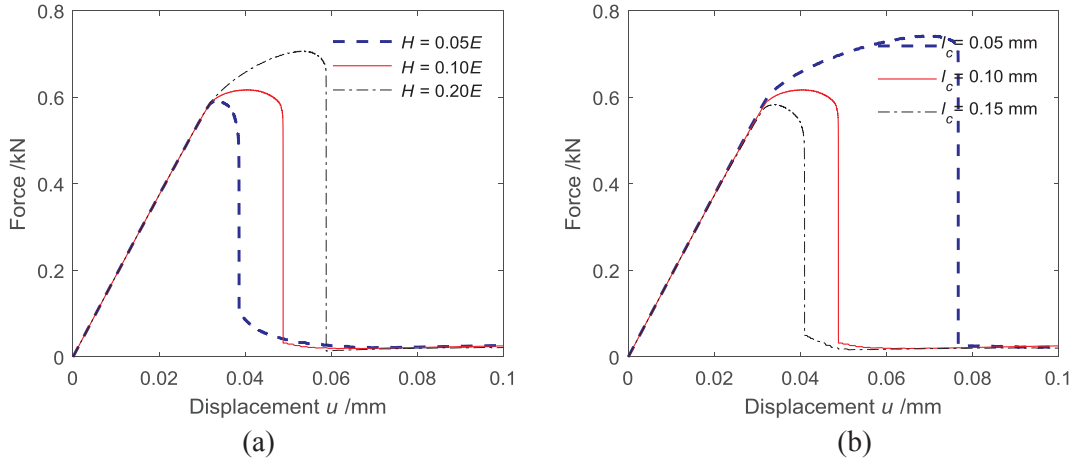

Fig. 12. Force versus displacement curve of the flat grooved specimen: (a) effect of hardening modulus; and (b) effect of the length scale parameter.

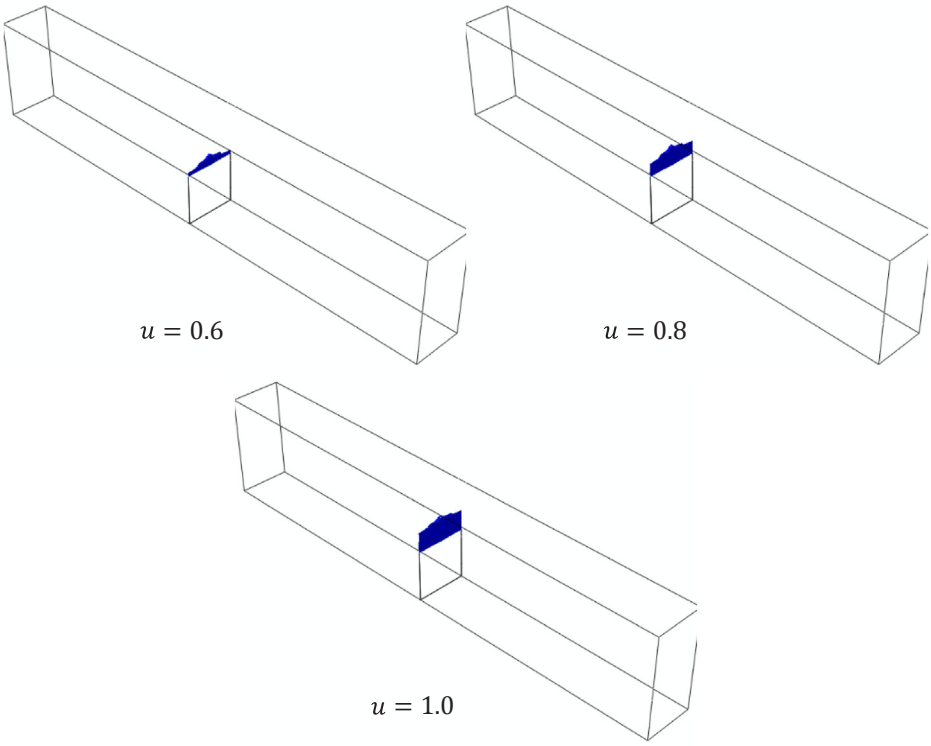

Fig. 15. Crack propagation of the 3D notched beam.

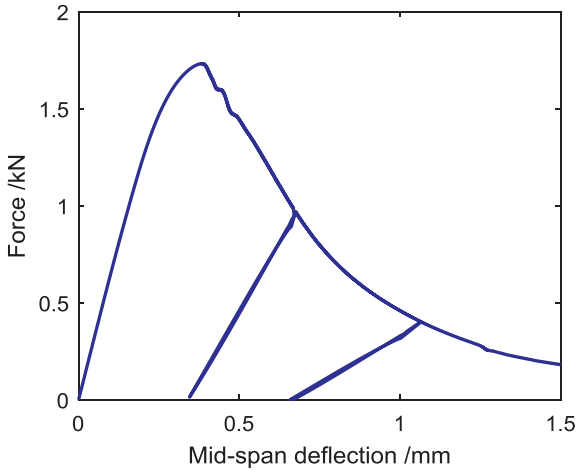

Fig. 16. Reaction force versus the mid-span deflection of the 3D notched beam.

because of coupling with plasticity.

4.6. Tension/ shear of a 3D single-edge notched specimen

We end this section with a 3D single-edge notched specimen as shown in Fig. 17. Two loading cases are considered here, namely pure tension ($u_x = 0, \quad u_y \neq 0$) and pure shear ($u_x \neq 0, \quad u_y = 0$). The loading increments are set to $\Delta u_y = 1.0 \times 10^{-4}$ mm and $\Delta u_x = 2.0 \times 10^{-4}$ mm, respectively. The spatial discretisation contains refinement in the region where the crack is expected to develop. The length scale parameter l_c is set to be 0.02 mm.

Fig. 18 illustrates the crack growth for the tension and shear loading cases, respectively, where the isosurface of the phase field damage is depicted with a value greater than 0.95. The crack propagates vertically under tension and shear loads. The prediction of crack paths is

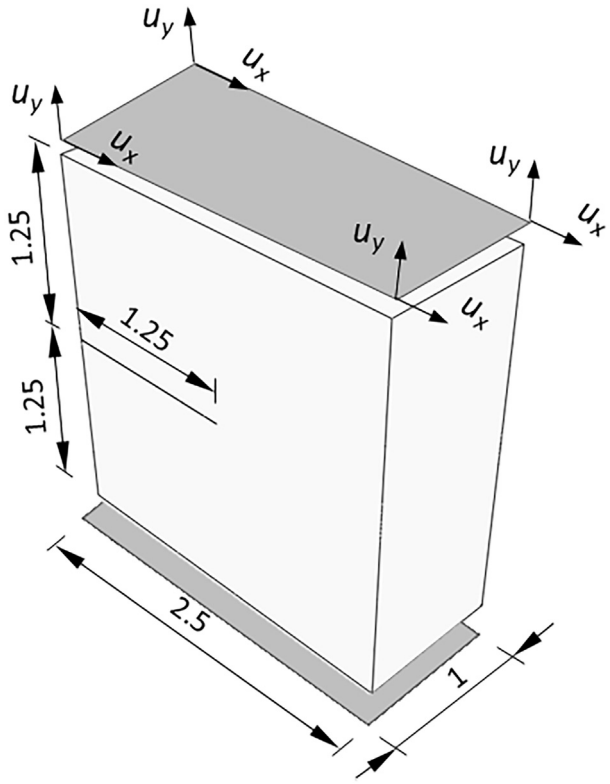

Fig. 17. Geometry of the 3D single-edge notched specimen.

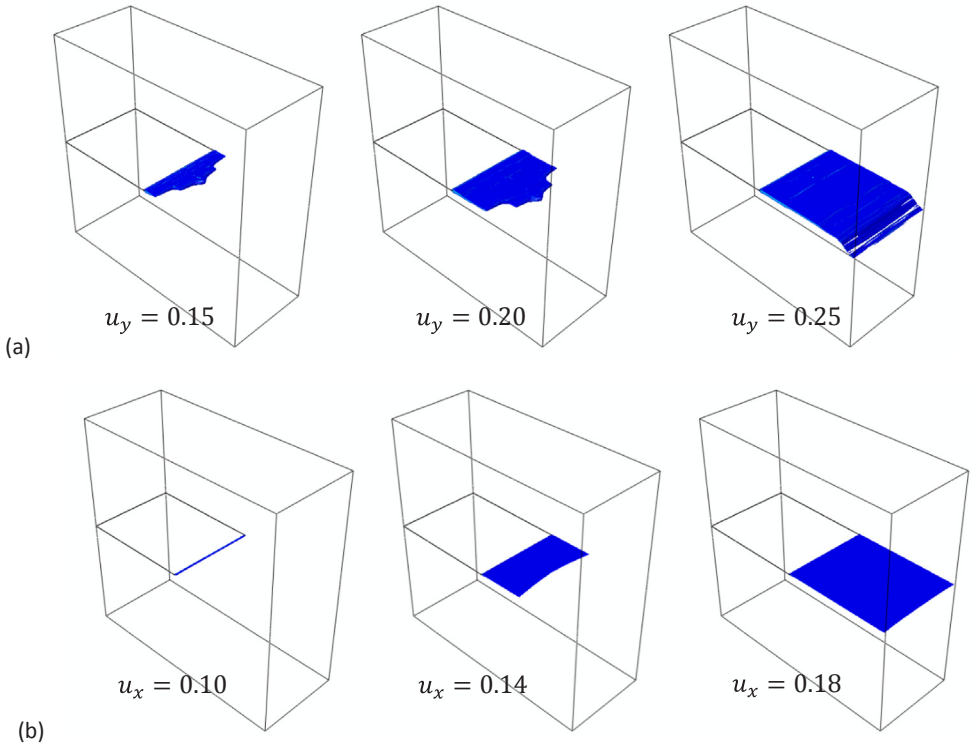

Fig. 18. Crack propagation of the 3D single-edge notched specimen: (a) pure tension; (b) pure shear.

consistent with the results in [38].

5. Conclusions

In this study, we present the implementation of phase field modelling for fracture in elasto-plastic solids in commercial finite element software Abaqus. The coupled system is solved using a staggered scheme via Abaqus subroutines UEL and a UMAT. The displacement field and phase field are decoupled and solved separately using the Newton Raphson iteration. Within each iteration, one field is computed by freezing the other field (and relevant internal parameters) at the last load increment.

A number of benchmark examples for fracture in elasto-plastic solids are tested, from one single element to 3D problems. We also study the effects of loading increment size, hardening, length scale parameter on the mechanical response of the problems. The correctness and effectiveness of the proposed implementation are demonstrated through these examples. Specifically, the staggered scheme is verified by comparing the numerical solution with the analytic solution in the one element example. From the 2D and 3D examples presented, the experimental observation and numerical results in the literature are reproduced in terms of reaction force and crack propagation.

The FORTRAN codes are accessible together with Abaqus input files from the link in Supplementary data. A tutorial is also provided in Appendix A to show how to solve fracture problems of elasto-plastic solids using the phase field method. The proposed implementation would be helpful only not for research academics but also for engineering practitioners to take advantage of phase field modelling for fracture of elasto-plastic solids.

Acknowledgements

This work was supported by The University of Technology Sydney (UTS), Australia through a Chancellor's Postdoctoral Research Fellowship and by Australian Research Council (ARC) through Discovery Projects (DP160104661 and DP190103752).

Appendix A. Tutorial

This section presents how to use the provided subroutine codes in Supplementary data to solve the problem of one 3D element subject to uniaxial tension as depicted in Section 4.1. The problem consists of two files: an Abaqus input file (*.inp) and a FORTRAN file (*.for). The Abaqus input file containing node and element information is generally written by a commercial pre-processor (e.g, Abaqus/CAE, Hypermesh). One can then use a code editor like Notepad++ to do some modifications to the input file.

After creating the nodes, the displacement-field element is generated for the first layer (*Element, TYPE = C3D8, elset = Displacement). It starts with the element number and then the node numbers (1, 5, 6, 8, 7, 1, 2, 4, 3). Following that, the user-defined material model is defined. 22 solution-dependent state variables in Table 2 are stored in UMAT and they can be post-processed in Abaqus/CAE. Six elasto-plastic material parameters are assigned: Young's modulus, Poisson ratio and yield stress versus equivalent plastic strain curve, which are passed to the UMAT subroutine.

The phase-field elements are defined for the second layer (*User element, nodes = 8, type = U1, properties = 2, coordinates = 3, VARIABLES = 24). This command defines an element with four nodes, in 3D, with two material properties and 24 state variables. The state variables are the phase-field value, elastic strain energy and plastic dissipation at each integration points as listed in Table 2. When generating the elements (*Element, type = U1, elset = Phase), the element node is shifted by NEL, which must be changed for each model, and the nodes must remain the same sequence, i.e., (**2**, 5, 6, 8, 7, 1, 2, 4, 3). After that, the properties for the second layer element is assigned (*Uel property, elset = Phase): length scale parameter l_c and fracture energy density g_f.

The rest of the input file is to define the loads, boundaries and analysis.

Appendix B. Supplementary material

Supplementary data to this article can be found online at https://doi.org/10.1016/j.tafmec.2019.102252.

The Supplementary should be linked to this data. https://data.mendeley.com/datasets/9n6rhvmjjn/1.

References

[1] G.L. Peng, Y.H. Wang, A Node Split Method for Crack Growth Problem. Applied Mechanics and Materials, Trans Tech Publ, 2012, pp. 1524–1528.
[2] F. Zhou, J.-F. Molinari, Dynamic crack propagation with cohesive elements: a methodology to address mesh dependency, Int. J. Numer. Meth. Eng. 59 (2004) 1–24.
[3] N.M. Azevedo, J. Lemos, Hybrid discrete element/finite element method for fracture analysis, Comput. Methods Appl. Mech. Eng. 195 (2006) 4579–4593.
[4] R. Mueller, G. Maugin, On material forces and finite element discretizations, Comput. Mech. 29 (2002) 52–60.
[5] C. Miehe, E. Gürses, M. Birkle, A computational framework of configurational-force-driven brittle fracture based on incremental energy minimization, Int. J. Fract. 145 (2007) 245–259.
[6] E. Gürses, C. Miehe, A computational framework of three-dimensional configurational-force-driven brittle crack propagation, Comput. Methods Appl. Mech. Eng. 198 (2009) 1413–1428.
[7] N. Moës, J. Dolbow, T. Belytschko, A finite element method for crack growth without remeshing, Int. J. Numer. Meth. Eng. 46 (1999) 131–150.
[8] N. Moës, A. Gravouil, T. Belytschko, Non-planar 3D crack growth by the extended finite element and level sets—Part I: Mechanical model, Int. J. Numer. Meth. Eng. 53 (2002) 2549–2568.
[9] T. Rabczuk, T. Belytschko, Cracking particles: a simplified meshfree method for arbitrary evolving cracks, Int. J. Numer. Meth. Eng. 61 (2004) 2316–2343.
[10] T. Rabczuk, T. Belytschko, A three-dimensional large deformation meshfree method for arbitrary evolving cracks, Comput. Methods Appl. Mech. Eng. 196 (2007) 2777–2799.
[11] T. Rabczuk, G. Zi, S. Bordas, H. Nguyen-Xuan, A simple and robust three-dimensional cracking-particle method without enrichment, Comput. Methods Appl. Mech. Eng. 199 (2010) 2437–2455.
[12] G.A. Francfort, J.-J. Marigo, Revisiting brittle fracture as an energy minimization problem, J. Mech. Phys. Solids 46 (1998) 1319–1342.
[13] B. Bourdin, G.A. Francfort, J.-J. Marigo, Numerical experiments in revisited brittle fracture, J. Mech. Phys. Solids 48 (2000) 797–826.
[14] C. Miehe, F. Welschinger, M. Hofacker, Thermodynamically consistent phase-field models of fracture: Variational principles and multi-field FE implementations, Int. J. Numer. Meth. Eng. 83 (2010) 1273–1311.
[15] M.J. Borden, C.V. Verhoosel, M.A. Scott, T.J. Hughes, C.M. Landis, A phase-field description of dynamic brittle fracture, Comput. Methods Appl. Mech. Eng. 217 (2012) 77–95.
[16] M. Hofacker, C. Miehe, Continuum phase field modeling of dynamic fracture: variational principles and staggered FE implementation, Int. J. Fract. 178 (2012) 113–129.
[17] A. Karma, D.A. Kessler, H. Levine, Phase-field model of mode III dynamic fracture, Phys. Rev. Lett. 87 (2001) 045501.
[18] H. Henry, H. Levine, Dynamic instabilities of fracture under biaxial strain using a phase field model, Phys. Rev. Lett. 93 (2004) 105504.
[19] C. Miehe, M. Hofacker, F. Welschinger, A phase field model for rate-independent crack propagation: Robust algorithmic implementation based on operator splits, Comput. Methods Appl. Mech. Eng. 199 (2010) 2765–2778.
[20] C. Kuhn, R. Müller, A continuum phase field model for fracture, Eng. Fract. Mech. 77 (2010) 3625–3634.
[21] C. Miehe, L.-M. Schaenzel, H. Ulmer, Phase field modeling of fracture in multi-physics problems. Part I. Balance of crack surface and failure criteria for brittle crack propagation in thermo-elastic solids, Comput. Methods Appl. Mech. Eng. 294 (2015) 449–485.
[22] S. Zhou, X. Zhuang, H. Zhu, T. Rabczuk, Phase field modelling of crack propagation, branching and coalescence in rocks, Theor. Appl. Fract. Mech. 96 (2018) 174–192.
[23] P. Areias, T. Rabczuk, M. Msekh, Phase-field analysis of finite-strain plates and shells including element subdivision, Comput. Methods Appl. Mech. Eng. 312 (2016) 322–350.
[24] F. Amiri, D. Millán, Y. Shen, T. Rabczuk, M. Arroyo, Phase-field modeling of fracture in linear thin shells, Theor. Appl. Fract. Mech. 69 (2014) 102–109.
[25] L. Xia, D. Da, J. Yvonnet, Topology optimization for maximizing the fracture resistance of quasi-brittle composites, Comput. Methods Appl. Mech. Eng. 332 (2018) 234–254.
[26] C. Wu, J. Fang, S. Zhou, G. Steven, Q. Li, Level-set topology optimization for maximizing fracture resistance of brittle materials using phase field fracture model, Comput. Methods Appl. Mech. Eng. (2019) (submitted for publication).
[27] M.A. Msekh, J.M. Sargado, M. Jamshidian, P.M. Areias, T. Rabczuk, Abaqus implementation of phase-field model for brittle fracture, Comput. Mater. Sci. 96 (2015) 472–484.
[28] G. Molnár, A. Gravouil, 2D and 3D Abaqus implementation of a robust staggered phase-field solution for modeling brittle fracture, Finite Elem. Anal. Des. 130 (2017) 27–38.
[29] G. Liu, Q. Li, M.A. Msekh, Z. Zuo, Abaqus implementation of monolithic and staggered schemes for quasi-static and dynamic fracture phase-field model, Comput. Mater. Sci. 121 (2016) 35–47.
[30] S. Zhou, T. Rabczuk, X. Zhuang, Phase field modeling of quasi-static and dynamic crack propagation: COMSOL implementation and case studies, Adv. Eng. Softw. 122 (2018) 31–49.
[31] K. Seleš, T. Lesičar, Z. Tonković, J. Sorić, A residual control staggered solution scheme for the phase-field modeling of brittle fracture, Eng. Fract. Mech. 205 (2019) 370–386.
[32] E. Pramono, K. Willam, Fracture energy-based plasticity formulation of plain concrete, J. Eng. Mech. 115 (1989) 1183–1204.
[33] W.F. Chen, A.F. Saleeb, Constitutive Equations for Engineering Materials: Plasticity and Modeling, Elsevier, 1994.
[34] C. Miehe, M. Hofacker, L.-M. Schänzel, F. Aldakheel, Phase field modeling of fracture in multi-physics problems. Part II. Coupled brittle-to-ductile failure criteria and crack propagation in thermo-elastic–plastic solids, Comput. Methods Appl. Mech. Eng. 294 (2015) 486–522.
[35] M. Hofacker, C. Miehe, A phase field model for ductile to brittle failure mode transition, PAMM. 12 (2012) 173–174.
[36] H. Ulmer, M. Hofacker, C. Miehe, Phase field modeling of brittle and ductile fracture, PAMM. 13 (2013) 533–536.
[37] F.P. Duda, A. Ciarbonetti, P.J. Sánchez, A.E. Huespe, A phase-field/gradient damage model for brittle fracture in elastic–plastic solids, Int. J. Plast. 65 (2015) 269–296.
[38] M. Ambati, T. Gerasimov, L. De Lorenzis, Phase-field modeling of ductile fracture, Comput. Mech. 55 (2015) 1017–1040.
[39] M.J. Borden, T.J. Hughes, C.M. Landis, A. Anvari, I.J. Lee, A phase-field formulation for fracture in ductile materials: Finite deformation balance law derivation, plastic degradation, and stress triaxiality effects, Comput. Methods Appl. Mech. Eng. 312 (2016) 130–166.
[40] R. Alessi, J.-J. Marigo, C. Maurini, S. Vidoli, Coupling damage and plasticity for a phase-field regularisation of brittle, cohesive and ductile fracture: one-dimensional examples, Int. J. Mech. Sci. (2017).
[41] R. Alessi, M. Ambati, T. Gerasimov, S. Vidoli, L. De Lorenzis, Comparison of phase-field models of fracture coupled with plasticity, Advances in Computational Plasticity, Springer, 2018, pp. 1–21.
[42] P. Rodriguez, J. Ulloa, C. Samaniego, E. Samaniego, A variational approach to the phase field modeling of brittle and ductile fracture, Int. J. Mech. Sci. (2018).
[43] J. Fang, C. Wu, J. Li, Q. Liu, C. Wu, G. Sun, et al., Phase field fracture in elasto-plastic solids: Variational formulation for multi-surface plasticity and effects of plastic yield surfaces and hardening, Int. J. Mech. Sci. 156 (2019) 382–396.
[44] J. Lee, G.L. Fenves, Plastic-damage model for cyclic loading of concrete structures, J. Eng. Mech. 124 (1998) 892–900.
[45] J.Y. Wu, J. Li, R. Faria, An energy release rate-based plastic-damage model for concrete, Int. J. Solids Struct. 43 (2006) 583–612.
[46] G.Z. Voyiadjis, Z.N. Taqieddin, P.I. Kattan, Anisotropic damage–plasticity model for concrete, Int. J. Plast. 24 (2008) 1946–1965.
[47] P. Grassl, D. Xenos, U. Nyström, R. Rempling, K. Gylltoft, CDPM2: A damage-plasticity approach to modelling the failure of concrete, Int. J. Solids Struct. 50 (2013) 3805–3816.
[48] T.-S. Cao, Numerical simulation of 3D ductile cracks formation using recent improved Lode-dependent plasticity and damage models combined with remeshing, Int. J. Solids Struct. 51 (2014) 2370–2381.